A Study on the Laser Spatter and the Oxidation Reactions During Selective Laser Melting of 316L Stainless Steel, Al-Si10-Mg, and Ti-6Al-4V

MARCO SIMONELLI, CHRIS TUCK, NESMA T. ABOULKHAIR, IAN MASKERY, IAN ASHCROFT, RICKY D. WILDMAN, and RICHARD HAGUE

The creation of an object by selective laser melting (SLM) occurs by melting contiguous areas of a powder bed according to a corresponding digital model. It is therefore clear that the success of this metal Additive Manufacturing (AM) technology relies on the comprehension of the events that take place during the melting and solidification of the powder bed. This study was designed to understand the generation of the laser spatter that is commonly observed during SLM and the potential effects that the spatter has on the processing of 316L stainless steel, Al-Si10-Mg, and Ti-6Al-4V. With the exception of Ti-6Al-4V, the characterization of the laser spatter revealed the presence of surface oxides enriched in the most volatile alloying elements of the materials. The study will discuss the implication of this finding on the material quality of the built parts.

DOI: 10.1007/s11661-015-2882-8

I. INTRODUCTION

In recent years, selective laser melting (SLM) has received great attention as a metal Additive Manufacturing (AM) technology that offers the possibility to rapidly manufacture metallic objects of great complexity generating little waste material. Research has shown that by using SLM, it is possible to realize open cell (lattice) structures, components with optimized structural topology, and custom-shaped objects in a variety of metallic materials such as stainless steel, aluminum, and titanium alloys.[1] For this reason, SLM has attracted the interest of communities operating in various fields such as the aerospace, automotive, and biomedical industries.[1]

The acceptance of SLM as a novel manufacturing technology depends, however, on the material quality of the printed objects and the repeatability intrinsic to the process. In recent years, great research efforts have been devoted to establish the relationship between the process, microstructure, and mechanical performance of printed parts.[2–5] The densification behavior, in particular, has been investigated to a great extent as residual porosity has been found to be detrimental to the tensile properties of the materials and one of the factors contributing to the poor fatigue resistance typical of the SLM materials.[5,6] Research has demonstrated that the density of the SLM parts can be increased by tuning four main process parameters: laser power, laser scan speed, hatch spacing, and powder layer thickness, or, in other words, the volumetric energy density that is delivered to the powder bed during the melting of each layer.[2–5] As each metal has a characteristic infrared laser absorbance and thermal properties, extensive experimental work is typically carried out to obtain a processing window that can lead to a production of high density parts. Another research approach to densification behavior is that of investigating the single track formation to find those process parameters that can produce uniform conduction mode melting and a sequence of stable melt pools.[7,8] Excellent correlation has been found between the conduction mode melting and the stability of the melt pool at single track level and density of the parts.[8]

Research has shown, however, that the melting regime and the melt pool stability also depend on the presence of oxides that might form during SLM. Considering the O_2 partial pressure typical of the SLM build chambers, it is likely that the high temperatures reached by the melt pool could trigger the formation of oxide films.[9] It is argued that the protective oxide layers of thickness in the nm size range, typical of metals such as stainless steel and titanium alloys, have a negligible effect on the SLM production, because they can be disrupted and stirred in the melt pool by the laser beam.[10] Instead, when thicker oxides are present, it is believed that the oxide layers cannot be completely disrupted (or vaporized) by the laser beam. In turn, the oxide residues deteriorate significantly the melting and the stability of the melt pool.[10] Oxide layers have indeed the tendency to lower the wetting of the substrate and thus induce balling of

MARCO SIMONELLI, Research Associate, CHRIS TUCK, Associate Professor, NESMA T. ABOULKHAIR, PhD Student, IAN MASKERY, Research Associate, IAN ASHCROFT, Professor of Mechanics of Solids, RICKY D. WILDMAN, Professor of Multiphase Flow and Mechanics, and RICHARD HAGUE, Professor of Innovative Manufacturing, and Director - EPSRC Centre for Additive Manufacturing, are with the University of Nottingham, Nottingham, U.K. Contact e-mail: marco.simonelli@nottingham.ac.uk
Manuscript submitted December 29, 2014.
Article published online April 4, 2015

the molten material, affect the fluid flow in the melt pool, and consequently the absorption of the laser energy, and impede uniform melting of the top deposited layer to the solid substrate below.[10–12] It is certain that for the typical energy inputs of SLM (in the order of 10^5 to 10^7 W/cm^2) a certain amount of evaporation of the metallic elements will occur.[9,13] The role of the material evaporation during SLM has been scarcely studied.[10] However, studies on laser welding have reported that the evaporation affects laser absorption, giving rise to the re-deposition of fumes inside the building chamber and contributes to the ejection of laser spatter from the melt pool.[14–17] Although the formation of the laser spatter is preceded by complex fluid flows, it has indeed been reported that the drag associated with the metallic vapor motion represents the main contribution to vertical momentum of the molten material before ejection.[14,15,17]

The analysis of the fraction of the laser spatter that falls on areas of the powder bed that are not scanned by the laser can provide important information regarding the oxidation reactions that occur during SLM because spatter originates directly from the melt pool. This research will study the laser spatter generated during the processing of three important materials mostly used in current metal AM: 316L stainless steel, Al-Si10-Mg, and Ti-6Al-4V. A thorough characterization of the laser spatter will thus help to clarify its generation and the effects that the laser spatter has on the quality of the parts produced by SLM.

II. MATERIALS AND METHODS

The SLM machine that was used for this work was a ReaLizer SLM50. The SLM50 operates in a protective atmosphere where Ar gas is constantly flushed across the build platform to minimize the oxidation reactions that might occur during the SLM process. The Ar gas flow also removes the laser plume and laser spatter away from the melt pool created by the laser. Although the ReaLizer SLM50 can operate with an oxygen level concentration up to 0.9 pct, in this work, the processing of the materials was carried out at an oxygen level of 0.2 pct, in order to minimize oxidation of the samples.

The SLM50 is equipped with a continuous 100W yttrium fiber laser (YLM-100-AC). The laser source operates at a wavelength $\lambda = 1.06$ μm and the nominal laser beam diameter can be condensed to a minimum spot size of 20 μm. In order to collect the same laser spatter that is generated during SLM, several cubic samples (125 mm^3) were built in AISI 316L stainless steel, Al-Si10-Mg, and Ti-6Al-4V. All the metallic powders that were used in this study were supplied by LPW Technology UK. Details on the gas atomized pre-alloyed AISI 316L stainless steel nominal composition are reported in Table I. The particles were mainly spherical with particle size distribution ranging from 5 to 50 μm. The second material that was used in the experiments was a pre-alloyed Ar gas atomized Al-Si10-Mg (the composition of this alloy is also listed in Table I). It is noteworthy that only a fraction of the powders had spherical shape and particles had prevalently irregular elongated shape.[4] The spherical fraction of powders was comprised between 30 and 50 μm. The third material used in the research was pre-alloyed plasma atomized Ti-6Al-4V (the composition of this alloy is also listed in Table 1). The particles were mainly spherical with particle size distribution comprised between 15 and 70 μm. Arbitrary samples of the metallic powders used in this research were investigated by scanning electron microscopy (SEM) to ensure that no contamination was present on the surface of the starting materials prior to SLM. The cubic samples were built with supporting structures automatically generated using the software package Magics (Materialise, Belgium) in order to ease the detachment of the samples from the build platform, at the completion of the building process. The build platform was kept at a temperature of 473 K (200 °C). The components were built on build platforms matching the material of the printed parts.

The cubic samples were built using a laser scan strategy that previous related research has shown to enable the production of high density parts (above 99.5 pct). The fiber laser initially scanned the borders of the square area corresponding to the cross section of the parts. In sequence, the square powder bed (inner area) was then scanned with an alternating parallel scan vector. In the case of Al-Si10-Mg and Ti-6Al-4V, the same layer was melted twice—using alternating scan vectors 90 deg rotated with respect to the first scan as it has been shown that the remelting can improve the density of the parts.[4] The laser processing parameters that were used in this study are summarized in Table II.

Under these processing conditions, a considerable amount of laser spattering was produced during the

Table I. Nominal Compositions of the Pre-alloyed Starting Materials Used in this Study

	Fe	Cr	Ni	Mo	Mn	Si	C	P	S	Cu
316L stainless steel	69.41	16.50	10.10	2.09	1.31	0.52	0.03	0.02	0.01	0.02
	Al	Si	Fe	Mg	Mn	Cu	Ni			
Al-Si10-Mg	89.26	9.71	0.50	0.41	0.06	0.05	0.02			
	Ti	Al	V	Fe	C	N	H			
Ti-6Al-4V	89.70	6.10	4.10	0.07	0.01	0.01	0.01			

Table II. Processing Conditions for the Three Materials Used in this Study

	Materials		
	316L Stainless Steel	Al-Si10-Mg	Ti-6Al-4V
Layer thickness (μm)	25	40	40
Scan strategy	alternate	alternate	alternate
No. of scans per layer	1	2	2
Laser power (W)			
Border	37.5	100	40
Inner area	82.5	100	82.5
Laser scan speed (mm/s)			
Border	250	250	250
Inner area	500	250 and 500*	500

*The inner cross section was scanned at 250 mm/s (first scan) and then 500 mm/s (second scan).

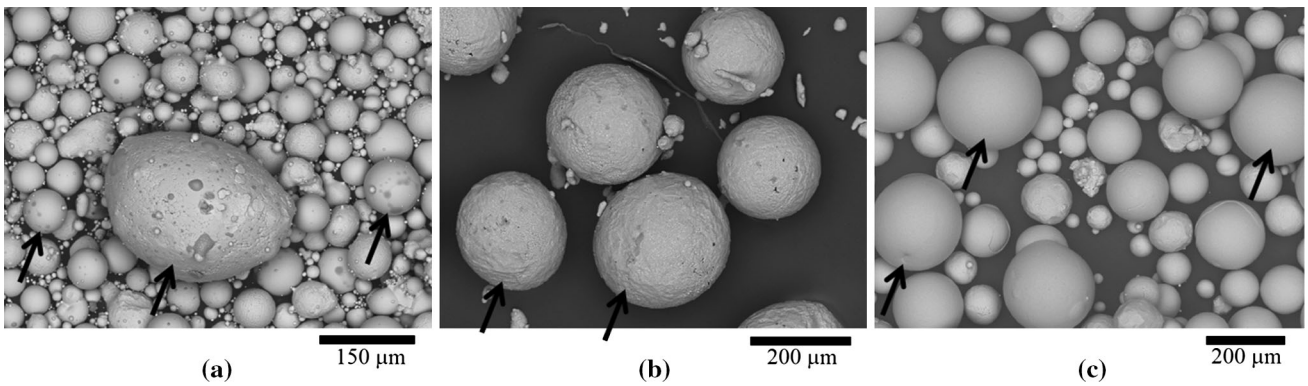

Fig. 1—Backscatter images showing (*a*) the 316L stainless steel, (*b*) the Al-Si10-Mg, and (*c*) the Ti-6Al-4V starting powders (feedstock material) and the laser spatter that has originated during SLM; the black arrows indicate examples of laser spatter particles.

melting of each layer of powders. The laser spatter was visible with the naked eye in the form of dark large particles accumulated in the proximity of the cross sections being processed. At the completion of the building process, the laser spatter floating on top of the loose powder bed was collected using C tabs. Pressing the C tab on the laser spatter ensured that copious amounts of laser spatter could be investigated and directly compared to the starting powders unaffected by the laser.

The characterization of the laser spatter generated during SLM and its comparison with the starting powders was conducted on two SEM systems: a Hitachi TM3030 and a FEI Nova 600 Nanolab Dualbeam FIB/FEG-SEM. The TM3030 was employed to image and identify compositional differences on the laser spatter external surface. The Nanolab Dualbeam FIB/FEG-SEM system was instead used to carry out *in situ* ion milling and investigate the bulk microstructure and composition of the starting powder materials and the corresponding laser spatter generated during SLM. The ion beam of the Nanolab Dualbeam FIB/FEG-SEM system can be focused to approximately 7 nm, therefore ion channeling contrast can be used to delineate the grain structure in the polycrystalline samples examined in this study. Prior to ion milling, the particles were Au coated to minimize image drifting that could occur on poorly conducting materials such as metallic powders. Energy-dispersive X-ray spectroscopy (EDS) mapping was used to characterize the microstructure of the particles and as a tool to discern the different phases, and the potential segregates and oxides layers.

III. RESULTS

Figure 1 shows that the collected samples consist of starting powders, *i.e.*, loose metallic powders that have not been laser melted, and laser spatter particles identified as particulate larger than the initial feedstock. The observed spatter ranged between 45 and 250 μm for 316L stainless steel, 110 and 330 μm for Al-Si10-Mg, and 130 and 270 μm in the case of Ti-6Al-4V (Figure 1). The spherical shape of the spatter is instead indicative of the fact that it originated, regardless of the metal alloy, as a molten metal that solidified in flight before impinging on the powder bed. Figure 1 also shows that the surface of the spatter of 316L stainless steel and Al-Si10-Mg contains dark patches, suggesting a difference in composition (the images were acquired using a backscatter detector, higher brightness corresponds to higher atomic number).

To investigate the role of the oxygen during SLM and discuss the effect of the laser spatter on the processability of the chosen materials, it was decided to compare the starting particles (feedstock material) directly with the laser spatter generated during SLM.

Figure 2(a) shows a cross section of a randomly chosen 316L stainless steel particle (feedstock material). The microscopy analysis revealed that the particle consisted of a single fully austenitic phase (fcc, face-centered cubic). 316L has in fact sufficient level of Ni to retain the austenitic phase structure up to its melting temperature.[18] Recent research on starting gas atomized 316L stainless steel has reported consistent results with the present findings.[19] The grains shown in Figure 2(a) have irregular shape and an equivalent diameter of few μm. The EDS analysis carried out on the same cross section (Figure 2(b)) reveals that the alloying elements are in full solid solution with no intergranular precipitates. This is indicative of the fact that during gas atomization the powders have solidified under rapid cooling rate.

Figure 3(a) shows the microstructure of one the laser spatter particles indicated in Figure 1(a). Similar to the starting powders, the laser spatter consists of a single austenitic phase. Figure 3(a) shows that spatter has a coarse microstructure with mainly equiaxed grains. The corresponding EDS analysis shows some extent of grain boundary segregation Cr, Mo, and Mn. The average coarser grain structure and the segregation observed in microstructure of the laser spatter are indicative of the fact that the laser spatter has formed under a relatively slower cooling rate than that of gas atomized powders. Although both gas atomized and spatter particles are solidified in a similar room temperature, inert environment, the laser spatter has a higher thermal mass and therefore it is plausible that the spattered particles are subject to a slower cooling rate.

The dark patches present on the surfaces of the laser spatter were then investigated (Figure 4). The EDS analysis revealed indeed that the dark areas are rich in Mn, Si, and O in comparison to the remaining surface of the spatter particles suggesting that the dark areas consist of a combination of Mn and Si oxides. Since the X-ray generation region for the elements of interest extends in the specimen to approximately 1 μm, it is however possible that the shown EDS maps are affected by a contribution from the laser spatter matrix underneath the feature of interest.

In order to obtain a more realistic composition of these areas and assess the thickness that the oxides can reach, it was decided to cross section one of these features. Figure 5(a) shows an ion beam image of the corresponding cross section. Figure 5(a) shows that the oxide spans over several grains and reaches a maximum thickness of about 5 μm. The EDS analysis confirms that these areas are indeed rich in Mn, O, and Si.

A similar comparative analysis was then conducted on Al-Si10-Mg. The microstructure of the starting Al-Si10-Mg powders (feedstock material) was not homogeneous (Figure 6(a)). Figure 6(a) shows an outer shell with a microstructure consisting of fine sub-micron grains. The cross section also highlights an internal core consisting of larger cellular grains. The shell and inner core are delineated by extensive cracking. EDS analysis shown in Figure 6(b) reveals that Al was present over the entire particle and no intermetallic compounds (such as Mg_2Si) were distinguishable. Si-rich areas can instead be discerned in the inner core of the particle. Given the morphology of the grain structure and the EDS, it is likely that the shell consists of primary Al grains (α-face-centered cubic) rich in Si that form upon quenching. Although not clear in Figure 6, it is likely that a thin layer of Si phase (β-diamond-like lattice) is present at the primary α grains boundaries as typical of quenched hypoeutectic Al-Si alloys.[5] The core consists of primary α grains surrounded by a matrix of eutectic composition ($\alpha + \beta$). The larger size of the primary α grains in the inner core indicates that this area has solidified under less rapid cooling rates compared to the outer shell. The absence of a complex dendritic structure of the primary α grains and the absence of plate-like grains in the

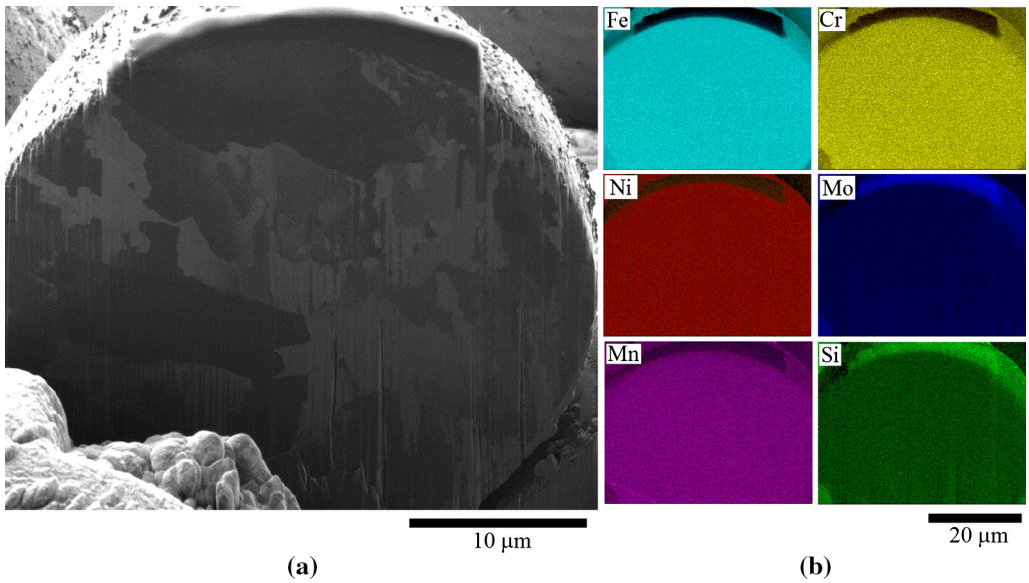

Fig. 2—(*a*) FIB image showing the grain structure of the 316L stainless steel starting powders; (*b*) EDS maps indicating the distribution of the alloying elements in the microstructure.

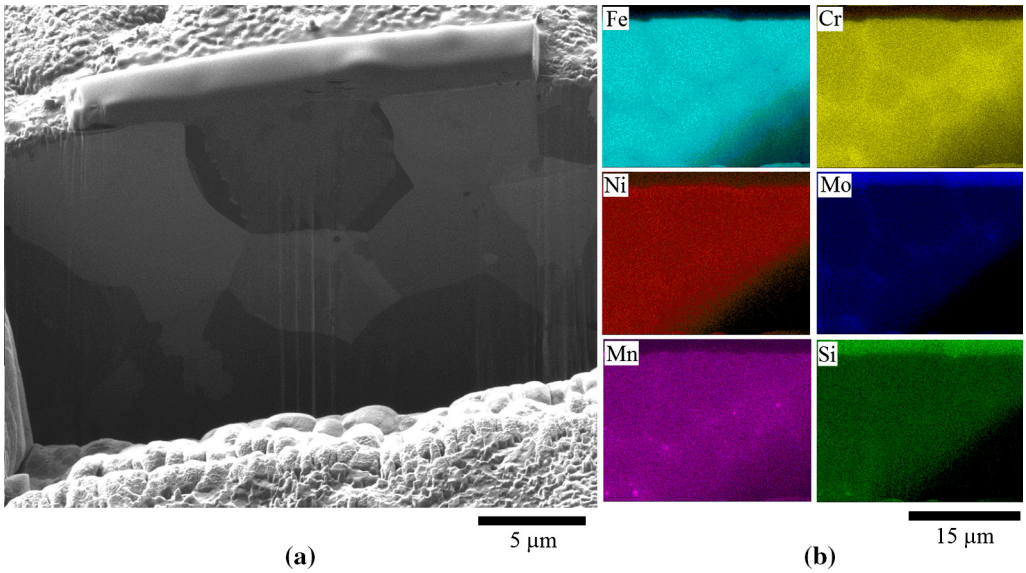

Fig. 3—(*a*) FIB image showing the grain structure of the 316L stainless steel laser spatter; (*b*) EDS maps indicating the distribution of the alloying elements in the microstructure.

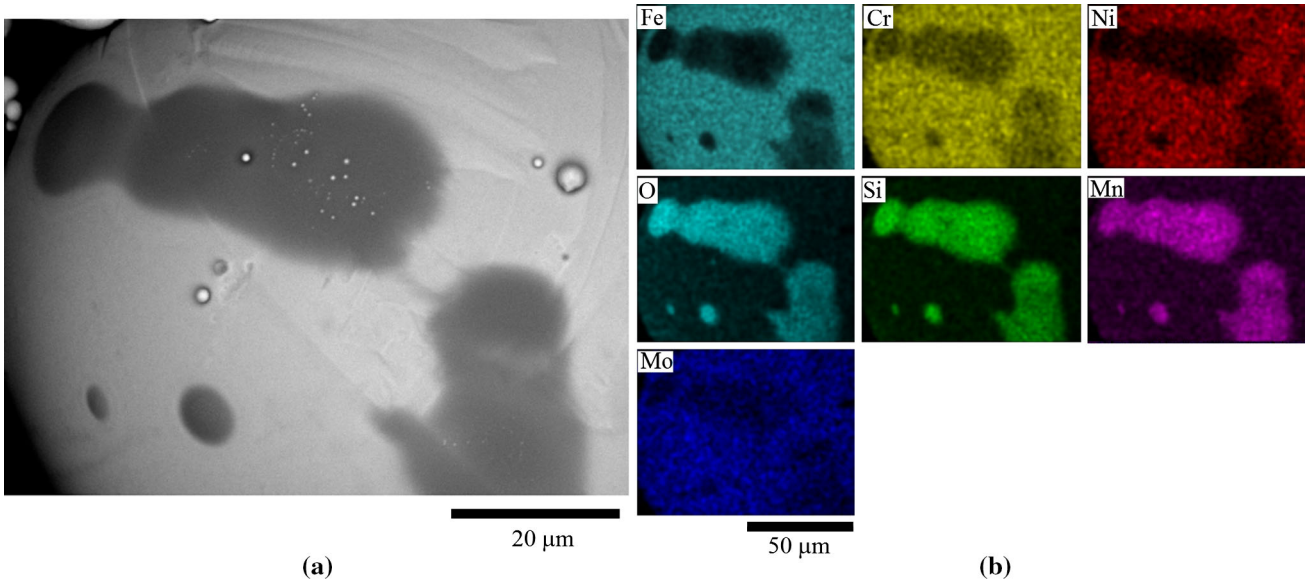

Fig. 4—(*a*) Backscatter image showing the oxide patches on the surface of the 316L stainless steel laser spatter; (*b*) EDS maps indicating the distribution of the alloying elements in the surface oxides.

eutectic matrix reveals, however, that also the outer core has solidified under high cooling rates.

Figure 7(a) shows the morphology of the Al-Si10-Mg laser spatter. The spatter is much larger than the starting powders and is mainly spherical.

The microstructure of the spatter is homogeneous as shown in Figure 7(a). The cross section shows that the microstructure consists of dendritic grains surrounded by a bi-phasic matrix. No internal cracking is visible in the cross section. The EDS analysis (Figure 7(b)) reveals that again Al is present over the entire particle cross section and no intermetallic compounds (such as Mg_2Si) are distinguishable. From the grain structure and EDS analysis, it is possible to conclude that the microstructure is made of primary α phase (dendritic grains) and a eutectic matrix composed of $\alpha + \beta$ phase. The α grains formed below the eutectic temperature are the grains with bright contrast in the matrix. No traces of oxides were found in the bulk microstructure of the laser spatter.

The dark areas on the surface of the Al-Si10-Mg spatter were then investigated. The microscopy and EDS analysis confirmed that—as in the case of 316L stainless steel—these areas are surface oxides. Figure 8(a) shows an example of the oxide layers found on the surface of the Al-Si10-Mg laser spatter. The compositional analysis reveals that the oxide is particularly rich in Mg, as shown in Figure 8(b).

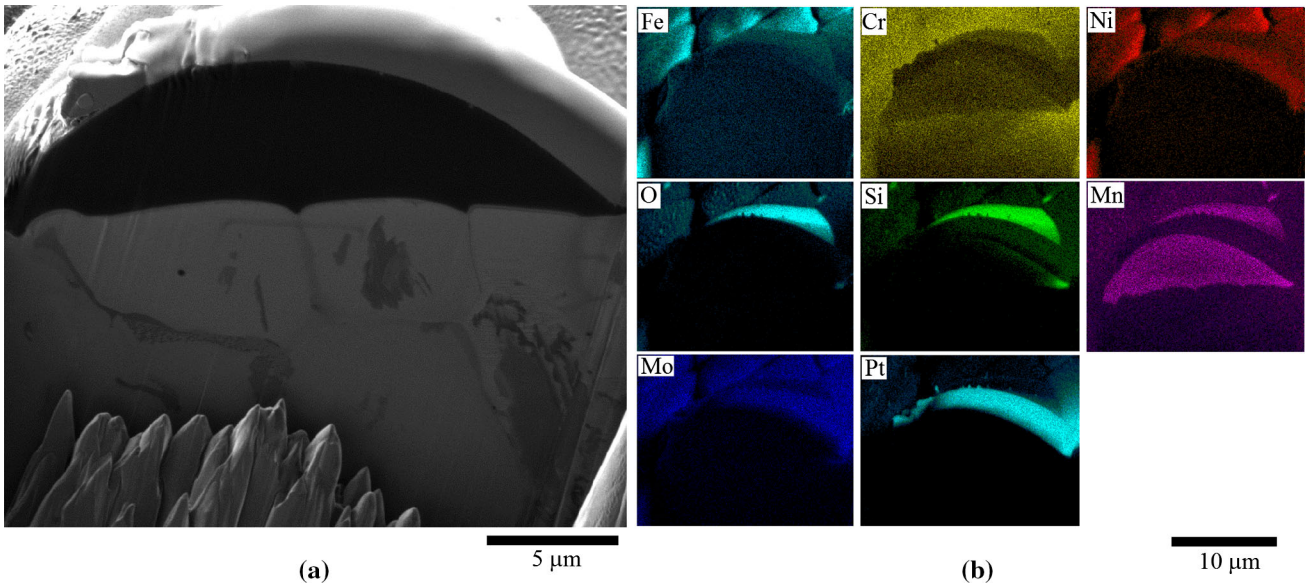

Fig. 5—(*a*) FIB image showing the cross section of an arbitrary oxide found on the surface of the 316L stainless steel laser spatter; (*b*) EDS maps indicating the distribution of the alloying elements in the oxide.

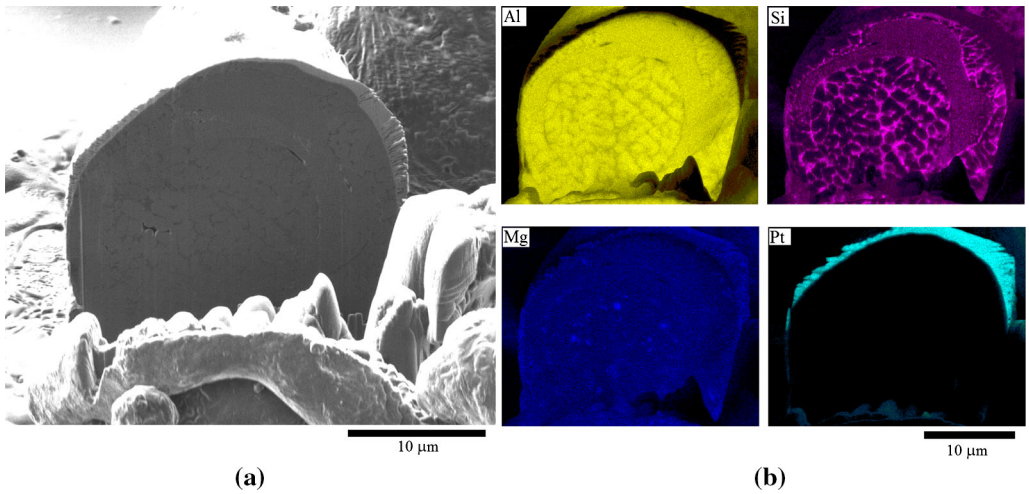

Fig. 6—(*a*) FIB image showing the grain structure of the Al-Si10-Mg starting powders; (*b*) EDS maps indicating the distribution of the alloying elements in the microstructure.

The third and final material under investigation was Ti-6Al-4V. The microstructure of one arbitrary starting particle (feedstock material) was investigated (Figure 9). The grain structure is not resolved well probably because the grains are too small to provide ion beam channeling contrast. The same authors have shown in previous research that plasma atomized Ti-6Al-4V solidify in a single α phase with the typical lamellar morphology that results from the Burgers orientation relationship that holds the bcc, body-centered cubic to hcp, hexagonal close-packed solid phase transformation.[20] EDS analysis shown in Figure 9(b) reveals that all the elements are in full solid solution, similarly to that observed in the case of gas atomized 316L stainless steel.

The microstructure of one arbitrary particle of laser spatter (Figure 10(a)) was then investigated. Similarly to that observed in the case of plasma atomized powders, the ion beam image has poor contrast, indicating a small grain structure and no areas of composition difference in the bulk of the spatter. The EDS analysis shown in Figure 10(b) reveals that all the elements are in full solid solution. In contrast to that observed for the other investigated materials, the Ti-6Al-4V laser spatter does not display any areas of compositional difference. The laser spatter surface presents no oxides on its surface, or its bulk microstructure. Figure 11 shows that the microstructure of the Ti-6Al-4V laser spatter consists entirely of α with no retained β phase.

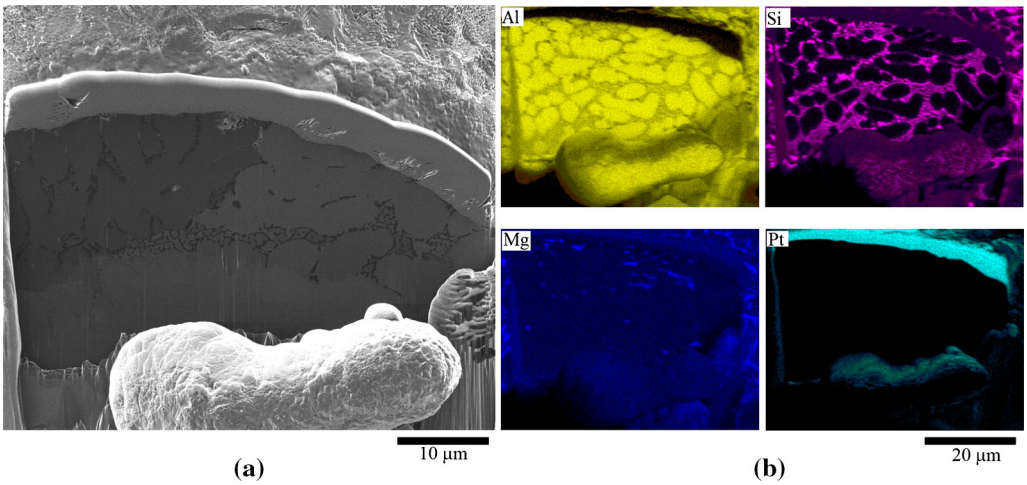

Fig. 7—(*a*) FIB image showing the grain structure of the Al-Si10-Mg laser spatter; (*b*) EDS maps indicating the distribution of the alloying elements in the microstructure.

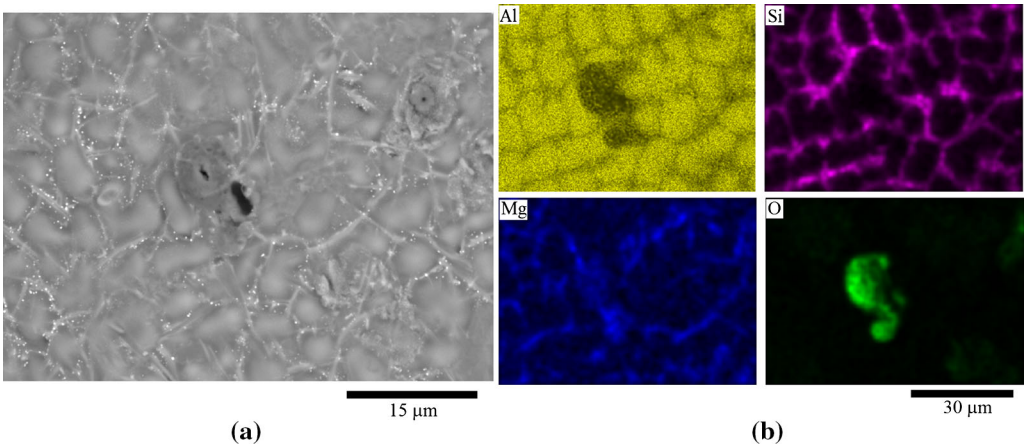

Fig. 8—(*a*) Backscatter image showing an oxide island on the surface of Al-Si10-Mg laser spatter; (*b*) EDS maps indicating the distribution of the alloying elements in the oxide.

IV. DISCUSSION

It is likely that the laser spatter formation during SLM is associated to the overheating of the melt pool, similar to that reported for conductive mode laser welding.[17] Although conductive mode melting is less dramatic than keyhole mode melting, given the high power density of the impinging laser, steep thermal gradients across the melt pool can be expected.[8] The thermal gradients cause surface tension gradients capable of driving flow of molten metal from the middle of the melt pool to its colder edges (or in opposite direction, if surface active elements are present in the melt pool) where spontaneous balling up of the liquid matter occurs to minimize the surface energy of the liquid metal.[9,11] It is likely that the drops are then expelled upwards away from the melt pool as a consequence of the vapor pressure created by continuous vaporization of material.[13,15,16] This would explain why, even when process parameters lead to the formation of high density parts, intense laser spatter formation was still observed. In addition, the proposed mechanism would also explain the prevalent spherical morphology of the observed laser spatter, regardless of the material that is being processed.

As the laser spatter results directly from the melt pool, its characterization can also be helpful to investigate the role of oxygen in the SLM building chamber. Several research studies on the metallurgy of SLM parts have suggested that oxide layers are not visible in the examined parts because the laser would break and stir the oxides into the melt pool upon successive layer depositions.[5,10,21] Nevertheless, the evidence presented in this study shows that no oxides are present in the bulk microstructure of the laser spatter that is not affected by successive layer depositions. Patches of thick oxide layers found in 316L and Al-Si10-Mg laser spatter, form instead on the surface of the spatter drops. For this reason, it is believed that the spatter molten material is ejected predominantly in the form of molten metallic material and oxidizes afterward—while in flight—in the SLM building chamber.

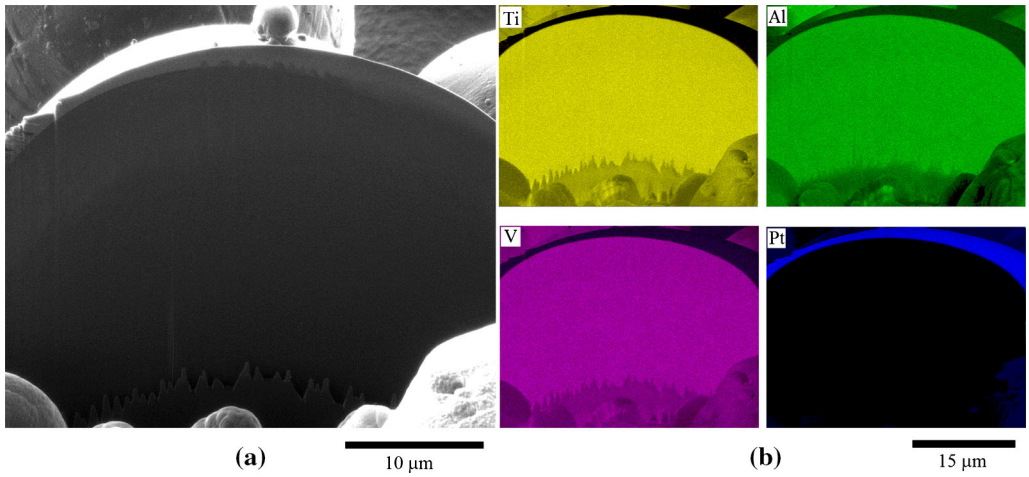

Fig. 9—(*a*) FIB image showing the cross section of a starting Ti-6Al-4V powder; (*b*) EDS maps indicating the distribution of the alloying elements in the microstructure.

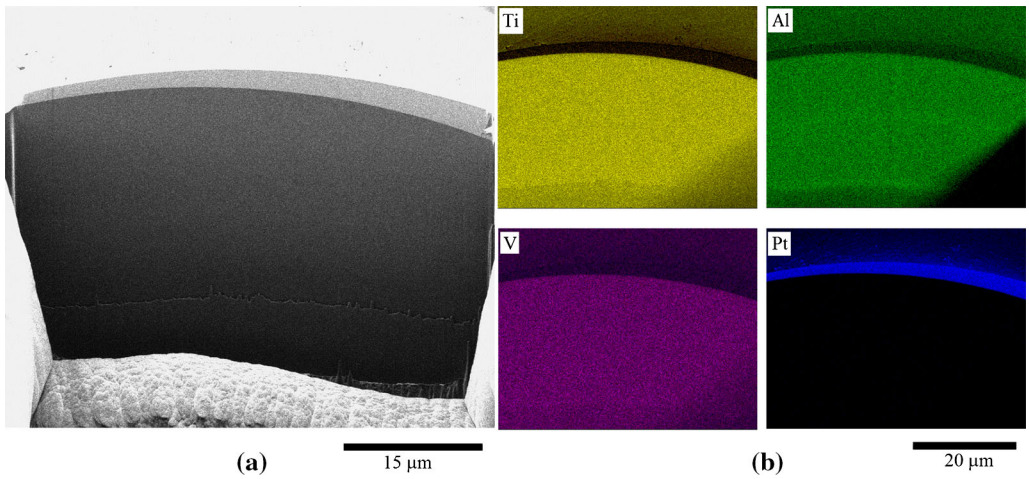

Fig. 10—(*a*) FIB image showing the cross section of a Ti-6Al-4V laser spatter; (*b*) EDS maps indicating the distribution of the alloying elements in the microstructure.

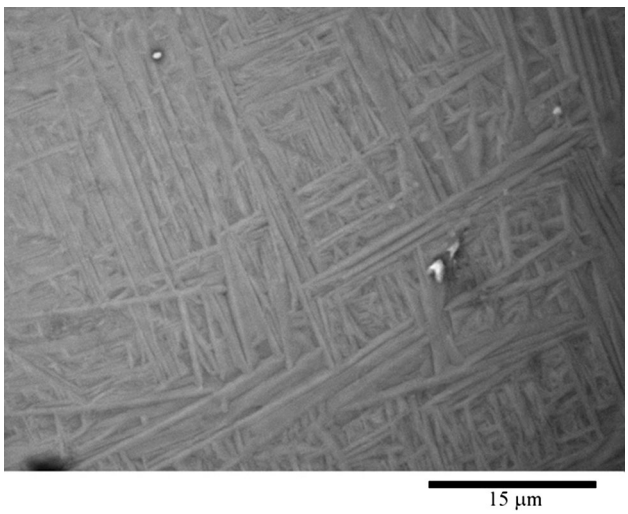

Fig. 11—Backscatter image showing the lamellar microstructure of the Ti-6Al-4V laser spatter.

The compositional analysis of the oxides found on the laser spatter shows selective oxidation of particular alloy elements, *i.e.*, predominately Mn (and Si) in 316L stainless steel and Mg in Al-Si10-Mg.

Research on steel powder metallurgy has shown that alloying elements with high affinity to oxygen, such as Mn and Si, can indeed be selectively oxidized on the powder surface when the powders are subjected to heat treatments.[22–24] Even in the case of pre-alloyed steel powders, it has been demonstrated that the powder surface is covered by heterogeneous oxide layers consisting of relatively uniform iron oxide layers (typical thickness below 10 nm) and several orders of magnitude thicker Mn and Si oxides.[23] The Ellingham diagram shows that the oxidation potential for Mn and Si elements are several orders of magnitude higher than Fe and Cr.[9,22] The high affinity to oxygen would then explain why Mn and Si selectively oxidize on the surface of 316L laser spatter. The exact reason behind the surface segregation of elemental alloys that sustain the growth of these thick surface oxides is unclear. Mn and

Si are present in small amounts in the pre-alloyed starting material, and the microstructural analysis of the laser spatter shows that the spatter is a single austenitic phase—therefore, Mn surface segregation cannot be explained in terms of phase partitioning. In addition, it seems that the oxides location is not correlated to grain boundary segregation—as the oxides examined in Figure 5(a) which span across multiple grains.

Studies on the evolution of the surface composition during steel annealing have reported the tendency of Mn to diffuse from the matrix toward the surface of the alloy.[25–27] It was suggested that Mn surface enrichment is promoted by the high volatility,[28] and high diffusion rate of Mn in the steel and particularly the austenitic phase structure. The presence of oxygen in the annealing chamber would then encourage the formation of the oxides, lowering the partial pressure of these elements in the chamber and thus encouraging further diffusion of the elements toward the surface.

Consistent with these observations, it is then not surprising that the oxide island shown in Figure 8(a) is enriched in Mg that, similarly to Mn, is a volatile element with strong affinity to oxygen.[10] In addition, silicon oxide films tend to have protective nature compared to Mg oxide films (*i.e.*, silicon oxides prevent oxygen diffusion into the underlying material) thus Mg oxide layers grow typically thicker than the former ones.[11,29] The reduced volatility of the alloying elements in Ti-6Al-4V would explain why no thick and visible oxides are present in the Ti-6Al-4V laser spatter.

Even if during SLM the material is molten for a very short time, it is plausible that the superheat of the liquid metal causes diffusion of the volatile elements toward the surface. Due to relatively high partial pressure of O_2 in the SLM chamber (typically comprised between 10^{-4} and 10^{-3} atm), the elements on the surface of the spatter with high affinity to oxygen will then form oxides layers with thickness in the μm range. On the other hand, gas and plasma atomization occurs in protective atmosphere with typical oxygen levels up to 100 ppm, therefore much lower than what occurs in SLM.[30] Because of the lower temperature reached by atomization, the faster cooling rates experienced by the particles, and the reduced pressure of oxygen in the process, only thin oxides (nm range) would form. These oxides, that can be studied with surface-sensitive techniques,[23,27,31] are however not visible during the metallurgical analysis conducted in this research.

Alternatively, the apparent surface segregation of Mn and Si might be a result of de-wetting and agglomeration of a thin uniform surface (molten) oxide formed on the surface of the spatter. In this way, the formation of the oxides would not have to involve bulk diffusion of Mn and Si to the surface of the spatter material. It is also noteworthy that oxygen dissolves in Ti solid solution to significant concentrations (unlike Fe and Al alloys). This might explain why, although oxygen pick-up is occurring during powder bed fusion AM,[32] no stable oxides are present on the surface of the Ti-6Al-4V spatter.

The deleterious effects of oxides on the particle fusion in steel powder metallurgy are well documented.[23,28,33,34] Research has demonstrated that residual oxides on powder surface can act as barriers and inhibit inter-particles necks fusion, decreasing the overall density of the sintered parts and therefore their mechanical performance.[28] As it is inevitable that laser spatter will deposit on loose starting powder of the powder bed or on the layer just consolidated by the laser, it can be argued that the laser spatter generated during SLM could have a similar effect on the quality of the parts. The partial fusion of the laser spatter to the substrate upon successive depositions would represent indeed heterogeneous inclusions that can degrade the mechanical performance—especially the fatigue life—of the SLM parts. In addition, it could be argued that as SLM feedstock is recycled where possible, the oxide content may increase with repeated use. In the case of alloys without alloying elements of high volatility, such as Ti-6Al-4V, no thick oxides were observed. The laser spatter is however much larger than the starting metallic powders and thus its contamination on the powder bed will lead to irregular porosity introduced by improper powder spreading.[5] It can be understood that the formation of a rough surface caused by inhomogeneous laser melting introduces a chain effect that degrades the overall quality of parts, including potential jamming between the peaks of the metallic layer and the re-coater of the SLM.[35]

As a conclusive remark, it is noteworthy that the laser used in this work was continuous *i.e.*, the power density that is delivered to the powder bed remained constant throughout the laser scan. Research has shown, however, that a less aggressive heating regime can reduce the amount of plasma plume/spatter generated during the melting process.[36] As the absorptivity of metallic powders is significantly higher than solid bulk metals,[1] by adopting a scan strategy where the powder bed is initially sintered using low energy density and then re-melted using a higher energy density, it is likely to reduce the amount of spatter generated during SLM.

Finally, recent research has shown that by modulating the shape of the laser pulses, *i.e.*, distributing the laser power density over longer period of time, desirable melting could be achieved at lower laser power.[36] As the overheating of the melt pool that is responsible for the generation of spatter is proportional to the laser power, pulse laser shaping could be an interesting approach to reduce the spatter formation and improve the quality of the SLM parts.

V. CONCLUSIONS

In recent years, numerous studies have focused on improving the quality of the parts and level of density associated with the SLM production. In this regard, research has shown that a suitable combination of laser process parameters can lead to a production of near fully dense components. The comprehension of the reactions that occur in the melt pool, and in particular the role of oxygen in the build chamber during SLM, would however bring to a further optimization of the process. In this research, the laser spatter generated during the production of AISI 316L stainless steel, AlSi10-Mg, and Ti-6Al-4V was investigated. The laser

spatter originates as a consequence of the complex dynamics taking place in the melt pool and therefore it is a good descriptor of the possible oxidation reactions that occur during SLM. It was observed that, regardless of the material that was being processed, the laser spatter has a spherical morphology. In addition, the laser spatter is much larger than the starting pre-alloyed powders. It was found that on the surface of the laser spatter of 316L, an Al-Si10-Mg selective oxidation occurs. No oxides were observed in the bulk microstructure of the spattered material. The analysis of the results suggests that the formation of surface oxides is underpinned by surface enrichment of the most volatile element present in the alloy. If these elements have also a great affinity to oxygen, as in the case of Mn, Si, and Mg, oxides with a thickness of several μm can be formed. The laser spatter formed during the processing of Ti-6Al-4V contains no oxides, likely because the alloy has no alloying elements with high volatility.

Based on these findings, in order to optimize the density of the SLM parts, it is suggested that a less aggressive heating regime capable to reduce the amount of plasma plume/spatter generated during the melting process should be considered.

REFERENCES

1. N. Hopkinson, R. Hague, and P. Dickens: *Rapid Manufacturing: An Industrial Revolution for the Digital Age*, Wiley, Chichester, 2006, pp. 175–245.
2. B. Liu, R. Wildman, C. Tuck, I. Ashcroft, and R. Hague: *Proc. 23rd Annu. Int. Solid Free. Fabr. Symp.*, 2011, pp. 227–38.
3. J.K.L. Thijs, F. Verhaeghe, T. Craeghs, and J.V. Humbeeck: *Acta Mater.*, 2010, vol. 58, pp. 3303–12.
4. N.T. Aboulkhair, N.M. Everitt, I. Ashcroft, and C. Tuck: *Addit. Manuf.*, 2014, vols. 1–4, pp. 77–86.
5. N. Read, W. Wang, K. Essa, and M.M. Attallah: *Mater. Des.*, 2015, vol. 65, pp. 417–24.
6. M. Simonelli, C. Tuck, and Y.Y. Tse: *Mater. Sci. Eng. A*, 2014, vol. 616, pp. 1–11.
7. I. Yadroitsev, P. Krakhmalev, I. Yadroitsava, S. Johansson, and I. Smurov: *J. Mater. Process. Technol.*, 2013, vol. 213, pp. 606–13.
8. W.E. King, H.D. Barth, V.M. Castillo, G.F. Gallegos, J.W. Gibbs, D.E. Hahn, C. Kamath, and A.M. Rubenchik: *J. Mater. Process. Technol.*, 2014, vol. 214, pp. 2915–25.
9. S. Das: *Adv. Eng. Mater.*, 2003, vol. 5, pp. 701–11.
10. E. Louvis, P. Fox, and C.J. Sutcliffe: *J. Mater. Process. Technol.*, 2011, vol. 211, pp. 275–84.
11. E.O. Olakanmi: *J. Mater. Process. Technol.*, 2013, vol. 213, pp. 1387–1405.
12. X.J. Wang, L.C. Zhang, M.H. Fang, and T.B. Sercombe: *Mater. Sci. Eng. A*, 2014, vol. 597, pp. 370–75.
13. F. Verhaeghe, T. Craeghs, J. Heulens, and L. Pandelaers: *Acta Mater.*, 2009, vol. 57, pp. 6006–12.
14. M.J. Zhang, G.Y. Chen, Y. Zhou, S.C. Li, and H. Deng: *Appl. Surf. Sci.*, 2013, vol. 280, pp. 868–75.
15. D.K. Low, L. Li, and P. Byrd: *J. Mater. Process. Technol.*, 2003, vol. 139, pp. 71–76.
16. S. Li, G. Chen, S. Katayama, and Y. Zhang: *Appl. Surf. Sci.*, 2014, vol. 303, pp. 481–88.
17. A.F.H. Kaplan and J. Powell: *J. Laser Appl.*, 2011, vol. 23, pp. 1–8.
18. G. Krauss: *Steels: Processing, Structure and Performance*, Materials Park, OH, ASM International, 2005, pp. 495–534.
19. B. Liu: Doctoral Thesis, Loughborough University, 2013, pp. 148–50.
20. M. Simonelli: Doctoral Thesis, Loughborough University, 2014, pp. 76–82.
21. L. Thijs, K. Kempen, J.-P. Kruth, and J. Van Humbeeck: *Acta Mater.*, 2013, vol. 61, pp. 1809–19.
22. P.R. Wilson and Z. Chen: *Corros. Sci.*, 2007, vol. 49, pp. 1305–20.
23. E. Hryha, C. Gierl, L. Nyborg, H. Danninger, and E. Dudrova: *Appl. Surf. Sci.*, 2010, vol. 256, pp. 3946–61.
24. P.R. Wilson and Z. Chen: *Scripta Mater.*, 2005, vol. 53, pp. 119–23.
25. A.F. Smitll and R. Hales: *Met. Sci.*, 1975, vol. 9, pp. 181–84.
26. Y.F. Gong, S. Birosca, H.S. Kim, and B.C.D. Cooman: *J. Microsc.*, 2008, vol. 230, pp. 424–34.
27. H.J. Grabke, V. Leroy, and H. Viefhaus: *Iron Steel Inst. Jpn.*, 1995, vol. 35, pp. 95–13.
28. E. Hryha, E. Dudrova, and L. Nyborg: *Metall. Mater. Trans. A*, 2010, vol. 41A, pp. 2880–97.
29. J.J. Dunkley: *Powder Metal Technologies and Applications*, ASM International, Materials Park, OH, 1998, pp. 35–52.
30. N.S. Stoloff: *Wrought and Powder Metallurgy (P/M) Superalloys*, ASM International, Materials Park, OH, 1998, pp. 1478–1527.
31. H. Karlsson, L. Nyborg, and S. Berg: *Powder Metall.*, 2005, vol. 48, pp. 51–58.
32. S. Das, M. Wohlert, J.J. Beaman, and D.L. Bourell: *JOM*, 1998, vol. 12, pp. 17–20.
33. D. Chasoglou, E. Hryha, and L. Nyborg: *Mater. Chem. Phys.*, 2013, vol. 138, pp. 405–15.
34. A.V. Krajnikov, V.V. Likutin, and G.E. Thompson: *Appl. Surf. Sci.*, 2003, vol. 210, pp. 318–28.
35. R. Li, Y. Shi, Z. Wang, L. Wang, J. Liu, and W. Jiang: *Appl. Surf. Sci.*, 2010, vol. 256, pp. 4350–4256.
36. K.A. Mumtaz and N. Hopkinson: *J. Mater. Process. Technol.*, 2010, vol. 210, pp. 279–87.